UC San Diego
UC San Diego Previously Published Works

Title

Wide spectrum of neuronal and network phenotypes in human stem cell-derived excitatory neurons with Rett syndrome-associated MECP2 mutations

Permalink

https://escholarship.org/uc/item/8xq9276p

Journal

Translational Psychiatry, 12(1)

ISSN

2158-3188

Authors

Mok, Rebecca SF
Zhang, Wenbo
Sheikh, Taimoor I
et al.

Publication Date

2022

DOI

10.1038/s41398-022-02216-1

ARTICLE OPEN

Wide spectrum of neuronal and network phenotypes in human stem cell-derived excitatory neurons with Rett syndrome-associated *MECP2* mutations

Rebecca S. F. Mok[1,2], Wenbo Zhang[3], Taimoor I. Sheikh[4], Kartik Pradeepan [5], Isabella R. Fernandes[6], Leah C. DeJong [1,2], Gabriel Benigno[7], Matthew R. Hildebrandt [2], Marat Mufteev[1,2], Deivid C. Rodrigues [2], Wei Wei[2], Alina Piekna[2], Jiajie Liu[2], Alysson R. Muotri [6,8], John B. Vincent [4], Lyle Muller [7], Julio Martinez-Trujillo [5], Michael W. Salter[3,9] and James Ellis [1,2 ✉]

© The Author(s) 2022

Rett syndrome (RTT) is a severe neurodevelopmental disorder primarily caused by heterozygous loss-of-function mutations in the X-linked gene *MECP2* that is a global transcriptional regulator. Mutations in the methyl-CpG binding domain (MBD) of MECP2 disrupt its interaction with methylated DNA. Here, we investigate the effect of a novel *MECP2* L124W missense mutation in the MBD of an atypical RTT patient with preserved speech in comparison to severe *MECP2* null mutations. L124W protein had a limited ability to disrupt heterochromatic chromocenters due to decreased binding dynamics. We isolated two pairs of isogenic WT and L124W induced pluripotent stem cells. L124W induced excitatory neurons expressed stable protein, exhibited increased input resistance and decreased voltage-gated Na$^+$ and K$^+$ currents, and their neuronal dysmorphology was limited to decreased dendritic complexity. Three isogenic pairs of *MECP2* null neurons had the expected more extreme morphological and electrophysiological phenotypes. We examined development and maturation of L124W and *MECP2* null excitatory neural network activity using micro-electrode arrays. Relative to isogenic controls, L124W neurons had an increase in synchronous network burst frequency, in contrast to *MECP2* null neurons that suffered a significant decrease in synchronous network burst frequency and a transient extension of network burst duration. A biologically motivated computational neural network model shows the observed changes in network dynamics are explained by changes in intrinsic Na$^+$ and K$^+$ currents in individual neurons. Our multilevel results demonstrate that RTT excitatory neurons show a wide spectrum of morphological, electrophysiological and circuitry phenotypes that are dependent on the severity of the *MECP2* mutation.

INTRODUCTION

Rett syndrome (RTT) is a rare neurodevelopmental disorder affecting females that is primarily caused by heterozygous loss-of-function mutations in the gene *MECP2* [1]. RTT is characterized by early developmental regression leading to microcephaly, loss of language and motor skills, development of hand stereotypies, gait abnormalities, and in some cases autism-like behaviours, autonomic dysfunction and seizures [2]. *MECP2* is an X-linked gene that undergoes X chromosome inactivation (XCI) in female cells, resulting in mosaic expression of the wild-type (WT) and mutant *MECP2* alleles in RTT individuals that may alter symptom presentation in instances of non-random XCI [3, 4]. Although *MECP2* mRNA is ubiquitously expressed, MECP2 protein is found to be most abundant in neurons [5], where it binds methylated DNA to act as a global transcriptional regulator to repress or activate genes [6, 7]. A large number of RTT patient-associated *MECP2* missense mutations map to the Methyl Binding Domain (MBD) and disrupt the interaction with DNA required for proper MECP2 function [7]. A functional consequence of some MBD missense mutations is that they disrupt heterochromatin condensates that are predicted to play a role in disease pathways in RTT [8].

Human stem cell-derived neuron models of RTT have confirmed many cellular phenotypes observed in *Mecp2* mouse models and classic RTT patients [9–16]. In these studies, WT and *MECP2* point or null mutation ESCs and iPSCs were differentiated into Neural Progenitor Cells (NPCs) and then into electrically active cortical

neurons. They showed that RTT neuron morphology is affected when MECP2 is dysfunctional, exhibiting reduced soma area, dendrite length, branch complexity and number of excitatory synapses. When RTT neuron electrophysiological properties were investigated during patch-clamp experiments [11, 13, 14], they show decreased action potential numbers in response to current pulses, fewer calcium transients and reduced frequency of spontaneous or miniature excitatory post-synaptic currents (mEPSC). These studies consistently demonstrated that classic RTT neurons have decreased size, dendritic branching, excitability and impaired excitatory neurotransmission, together suggesting a neuronal maturation defect.

It has been shown in electrophysiological studies of mouse cortical slices and hippocampal cultures that *Mecp2* neurons have decreased mEPSC amplitude or frequency [17, 18]. This implies that decreased excitatory neuronal activity and alteration of activity-dependent gene expression regulated by MECP2 [19, 20] may alter circuit maturation dynamics and contribute to the observed RTT phenotypes. How these changes translate into patterns of activity across networks of neurons in the developing human brain remains poorly documented. Recent approaches using induced excitatory neurons cocultured with astrocytes on micro-electrode arrays (MEAs) now allow evaluation of the development of synchronous network activity and how that circuitry is affected in neurodevelopmental disorders [21–23]. It is possible that early activity patterns of synchrony in neuronal networks observed during early brain development are impacted by the identified changes in single neurons, and that the degree of the impact depends on the severity of *MECP2* mutations. Simulation models predicting in vivo alterations in circuitry have advanced rapidly and provide an exciting opportunity to predict human circuitry changes in vitro such as variations of synchronic activity patterns during development [24, 25].

In this work, we use a multilevel approach (molecular-cellular-network-modeling) to compare the phenotypes of iPSC-derived excitatory neurons from severe classic *MECP2* null mutations to those of an atypical RTT patient with the preserved speech variant. This variant is described as the milder form of RTT, and the patients have diagnostic criteria composed of hand stereotypies, milder reduction in hand skills allowing quite good hand skills, language recovery using single words or complex phrases, normal head circumference, and milder intellectual disabilities [26]. We report a novel missense mutation in the MECP2 MBD at L124W (c.371 T > G) in the atypical patient that has unknown molecular consequences on MECP2 heterochromatin association. We compared atypical L124W to severely affected *MECP2* null excitatory neurons and their respective isogenic controls. We investigated protein expression levels, single neuron structure and electrophysiological characteristics (e.g., input resistance, voltage-gated Na$^+$ and K$^+$ currents, action potential firing, and excitatory synaptic function), and neuronal network dynamics using MEA recordings. The results were integrated into a computational network model of spiking neurons. Our results reveal a range of RTT-associated heterochromatin binding, neuron morphology, electrophysiology and circuitry phenotypes depending on *MECP2* mutation severity. The computational model simulations further indicate that the observed changes in RTT network dynamics are likely attributable to changes in intrinsic adaptation currents in single neurons.

RESULTS

Limited heterochromatin disruption by MECP2 L124W protein
MECP2 is known to play a role in chromatin architecture [27]. The structure of crystallized human WT MECP2 MBD bound to the *BDNF* promoter [28] demonstrated that the location of L124 maps in close 3D proximity to R106 (Fig. 1A). According to RettBASE [29], a database of patient *MECP2* variants, both of these residues are

mutated in classic Rett syndrome patients to L124F and R106W, respectively. When these two variants were expressed as GFP fusions in mouse cells they disrupted heterochromatic chromocenters [30–32]. To investigate whether the novel L124W MBD missense mutation associated with the preserved speech atypical RTT patient disrupts heterochromatin similarly to L124F and R106W, we assessed its ability to bind and cluster chromocenters relative to WT (instead of null MECP2 variants which cannot be expressed as fusion proteins). In brief, we over-expressed MECP2-GFP fusions in C2C12 mouse myoblast cells, which have low levels of endogenous Mecp2. GFP colocalization with DAPI marked chromocenters was measured by confocal microscopy in cells with similar fluorescence intensities. WT showed distinctly formed chromocenter clusters with high colocalization of GFP and DAPI as expected, while R106W and L124F showed completely disrupted chromocenter clustering and indistinct GFP and DAPI colocalization (Fig. 1B). In contrast, the novel L124W mutation showed limited heterochromatin disruption characterized by unaffected chromocenter number and reduced chromocenter size (Fig. 1B, C). L124W also was more distributed through the nucleus than was WT, showing reduced colocalization of GFP with DAPI as measured by Pearson's correlation coefficient (PCC) (Fig. 1B, C).

To explore the binding dynamics of L124W protein, fluorescence recovery after photobleaching (FRAP) live-imaging was used to study MECP2 protein mobility [32]. WT and L124W MECP2-GFP fusion proteins were overexpressed in C2C12 cells, and following photobleaching of a single chromocenter focus, MECP2-GFP fusion protein signal recovered more rapidly in the L124W compared with the WT over time (Fig. 1D). L124W had a shorter half-life and larger available unbound mobile fraction to recover the bleached signal that suggests it has decreased binding dynamics with heterochromatin (Fig. 1E). Taken together with the partial impairments in chromocenter clustering, these results point towards a limited effect of L124W relative to L124F and R106W mutations on MECP2 heterochromatin condensates due to decreased binding dynamics.

Generation of MECP2 L124W iPSCs and *Ngn2*-derived excitatory neurons
As differences in genetic background and modifier genes contribute to RTT phenotype severity [33, 34], disease modeling strategies using isogenic WT cells that are reprogrammed at the same time as mutant cells, or derived from the same iPSC line by gene editing, provide the most precise controls for comparing to affected cells. The use of isogenic controls addresses variability observed across different WT controls especially in the context of network circuitry studies [35], and variability can be further addressed by comparing isogenic pairs of cells in different wells within the same MEA plate. By taking advantage of XCI in female somatic cells, we and others have generated isogenic pairs of RTT stem cell lines from a single reprogramming experiment. As described below, we first generated isogenic human iPSC bearing the L124W missense mutation. As controls, we chose *MECP2* null cells including isogenic lines derived from a d3-4 patient [10] and a homozygous *MECP2* null line derived by gene editing of the human ESC line WIBR3 [13] that cannot reactivate a WT allele (Fig. 1F). We also generated a third *MECP2* null isogenic pair using gene editing of the PGPC14 healthy control iPSC line because whole genome sequencing showed it has no known genomic variants associated with neurological disorders [36].

We generated iPSCs from the atypical RTT patient (CLT) harbouring a heterozygous *MECP2* c.371 T > G variant resulting in the L124W amino acid change. iPSCs were reprogrammed from patient fibroblasts using Sendai virus, and STR analysis verified the lines were derived from the fibroblasts. The lines were first assessed for XCI status using the androgen receptor (AR) endonuclease digestion assay to identify isogenic lines fully skewed to either the WT or L124W allele on the active X
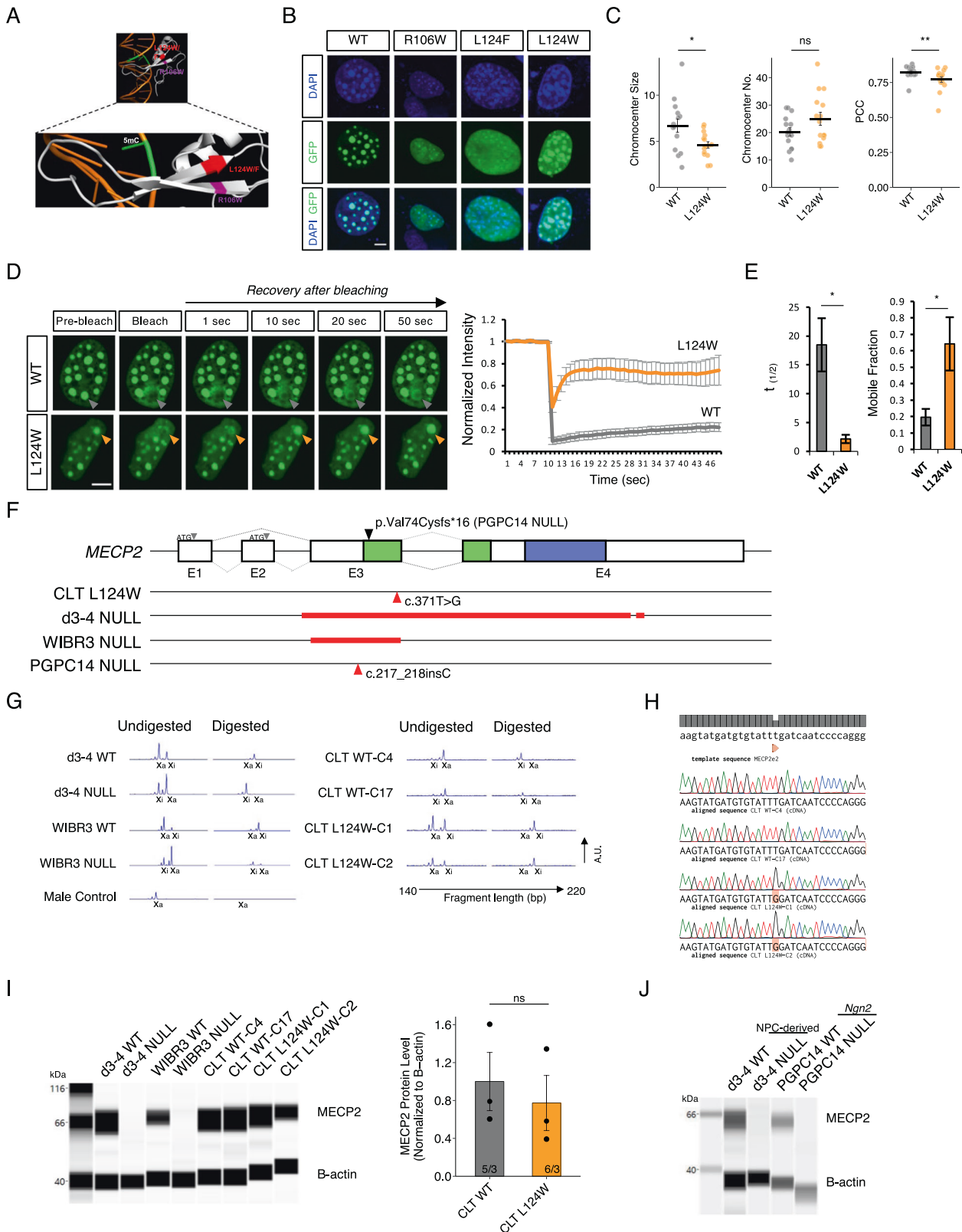
chromosome (X_a) with a male line as a control for full digestion of an unmethylated X_a (Fig. 1G). The terminology used for these CLT isogenic cell lines is CLT-WT and CLT-L124W. Two lines of X_a CLT-WT (C4 and C17) and two lines of X_a CLT-L124W (C1 and C2) were obtained with normal 46XX karyotype (Fig. S1A). The iPSC lines

demonstrated pluripotency by positive staining for OCT4, NANOG, SSEA-4 and TRA-1-60 (Fig. S1B), spontaneous differentiation into the 3-germ layers (Fig. S1C) and pluripotent cell expression profiles determined by RNA-seq and Pluritest analysis [37] (Fig. S1D). After this continued passage for pluripotency characterization, restricted

Fig. 1 Molecular impact of MECP2 L124W missense mutation and generation of iPSC lines. A MECP2 MBD 3D structure modeling L124W point mutation position relative to R106W. Human MECP2-MBD crystallographic structure illustrated using PyMol Molecular Graphic System (PDB accession code: 3C2I) showing MBD bound at methylated double stranded DNA sequence of *BDNF* promoter. **B** Representative images of C2C12 mouse myoblast cells overexpressing WT-GFP and mutant MECP2-GFP fusion proteins stained with DAPI (blue) and GFP (green). Scale bar = 2 μm. **C** Quantification of relative chromocenter size and number and overlap by Pearson's correlation co-efficient (PCC). $n = 15$ cells measured from 3 wells per condition. **D** Representative images of FRAP time course for GFP and quantified fluorescence intensity of WT-GFP and L124W-GFP in C2C12 mouse cells. Scale bar = 2 μm. **E** Quantification of WT-GFP and L124W-GFP half-life and mobile fraction. $n = 5$ cells measured from 3 wells per condition. **F** Schematic showing position of *MECP2* mutations in the iPSC/ESC lines used in this study. Red line indicates location of deletion and red arrow indicates location of the CLT point mutation or the PGPC14 null frameshift mutation in the gene. Black arrow indicates the PGPC14 null location of the early stop codon in the protein. Green indicates the methyl-binding domain and blue the transcriptional repression domain of MECP2 protein. **G** Amplified peaks from PCR of polymorphic androgen receptor locus on the X active (X_a) or X inactive (X_i) for endonuclease digested and undigested gDNA samples from WT and *MECP2* mutant iPSC lines. **H** Sanger sequencing of cDNA for the CLT WT or c.371 T > G (p.L124W) *MECP2* mutation from restricted expression of the active X chromosome in iPSC clones. **I** Digitized blot of isogenic *Ngn2* neurons and quantification of MECP2 protein level by capillary western in isogenic L124W *Ngn2* neurons normalized to β-actin. **J** Wes capillary-based protein detection of MECP2 protein in 6 week old PGPC14 WT and null *Ngn2* neurons, compared to 4 week old d3-4 WT and null NPC-derived neurons. All data were shown as mean +/− SEM, indicating n/N = number of samples/number of replicate batches. Statistical significance was evaluated by Student's *t*-test or Mann–Whitney test, as appropriate, in Fig. (**C**, **E** and **I**). ns $p > 0.05$, *$p < 0.05$, **$p < 0.01$.

mRNA expression of the X_a allele was again confirmed by cDNA sequencing across the L124W variant (Fig. 1H). In this way, the inactive X chromosome (X_i) was shown to not be subject to erosion [38] at two timepoints early in iPSC isolation and after full characterization just prior to differentiation of the lines into neurons.

To examine L124W protein levels in excitatory cortical neurons we used a rapid induced *Neurogenin-2* (*Ngn2*) overexpression protocol [39, 40] (Fig. S1E). In brief, WT and RTT iPSCs/ESCs were transduced with the Tet-inducible *Ngn2-puro* lentivirus vectors, overexpression was induced with doxycycline for 8 days and selected with puromycin in the presence of GDNF and BDNF, and dividing cells were eliminated with Ara-C prior to excitatory neuron re-plating and maturation. As expected, MECP2 capillary-based protein detection of 6 week old *Ngn2* neuron extracts demonstrated absence of MECP2 protein in d3-4 and WIBR3 null lines, but the levels of MECP2 protein were similar in isogenic CLT-WT and CLT-L124W lines (Fig. 1I). We conclude that L124W mutant protein is present and produced at unchanged levels in CLT-L124W cells.

While we proceeded to evaluate the CLT, d3-4 and WIBR3 neurons for neuronal activity as described in the next section, we used CRISPR/Cas9 gene editing to isolate a novel *MECP2* null line. We introduced indels into a previously characterized healthy control female PGPC14 iPSC line from the Personal Genome Project Canada [36]. PGPC14 iPSCs were co-transfected with Cas9 and a gRNA specific for exon 3 of *MECP2*. Selected clones were screened for normal karyotype (Fig. S1F) and found to be positive for hallmark pluripotency markers (Fig. S1G). cDNA sequencing identified a 1 bp insertion (c.217_218insC) into *MECP2* exon 3 on the X_a (Fig. S1H) of the PGPC14 null line, resulting in a frameshift and premature truncation of the protein (p.Val74Cysfs*16) early in the MBD (Fig. 1F). Generation of *Ngn2* neurons and protein detection by immunocytochemistry (Fig. S1I), capillary (Fig. 1J) and conventional western blot (Fig. S1J) demonstrated that PGPC14 indel neurons were *MECP2* null, compared with d3-4 null samples generated from NPC derived neurons, and neither null line reactivated the X_i to produce WT protein. The PGPC14 parental cells exhibit robust differentiation into many cell types, in contrast to the d3-4 lines, and were employed for subsequent neuron morphology and circuitry experiments.

RTT *Ngn2* neurons exhibit a range of alterations in intrinsic membrane properties and excitatory synaptic function

To validate *Ngn2*-derived excitatory neurons as an appropriate cellular model of RTT, we examined their electrophysiological characteristics and first determined whether there were detectable differences in the known *MECP2* null associated phenotypes. We made whole-cell patch-clamp recordings to investigate the intrinsic membrane properties of 4-5 week-old *Ngn2* neurons from isogenic d3-4 and WIBR3 *MECP2* null lines co-cultured with mouse astrocytes. We looked for alterations in electrophysiological characteristics as previously reported in mouse iPSC-derived neurons and human RTT neurons conventionally differentiated via an NPC stage [11, 41]. Indeed, relative to isogenic controls *MECP2* null neurons exhibited depolarized resting membrane potential, higher input resistance and decreased cell capacitance (Fig. 2A–C), consistent with the previous findings on RTT iPSC-derived neurons. We next assessed whether *MECP2* null mutant neurons had alterations in active membrane properties, as previously reported in RTT neurons [11, 41]. Voltage-gated Na$^+$ and K$^+$ currents, under voltage-clamp condition, were evoked by depolarizing voltage steps from a standardized holding potential of −70 mV. We found that both of Na$^+$ and K$^+$ currents were diminished in d3-4 and WIBR3 null neurons, compared with their respective isogenic WT (Fig. 2D). Given these alterations in the electrophysiological characteristics, *MECP2* null neurons were anticipated to have dysfunction in action potential firing. We therefore performed whole-cell current-clamp recordings to investigate the characteristics of action potentials, which were elicited by recording in current-clamp mode and injecting a series of current steps from −5 pA to 100 pA in both WT and *MECP2* null neurons (Figs. 2E & S2A–E). The majority of action potential parameters were not significantly different across the groups (Fig. S2A–E), dysfunction in the generation of action potentials was observed in *MECP2* null neurons as compared with the respective WT controls (Fig. 2E). Together, these findings indicate that loss of *MECP2* causes alterations in electrophysiological characteristics and deficiency in action potential firing, which may lead to a further influence on the functions of the neuronal network. We next examined synaptic transmission by recording mEPSCs in 6-week-old *Ngn2* WT and *MECP2* null neurons from d3-4 and WIBR3. We observed reduced AMPAR-mEPSC amplitude and frequency in the *MECP2* null neurons (Fig. 2F), consistent with previous reports of hypo-activity in RTT iPSC-derived cortical neurons [11, 41]. Taken together, these data indicate that *MECP2* null *Ngn2* neurons recapitulated known RTT-associated excitatory synaptic phenotypes.

Based on the limited disruption of heterochromatin condensates by L124W MECP2 protein, we predicted that CLT L124W *Ngn2* neurons would have a milder cellular phenotype in comparison to their isogenic WT neurons. In CLT L124W neurons the input resistance was greater than in the CLT WT neurons. However, neither resting membrane potential nor cell capacitance in CLT L124W neurons were different from those in CLT WT neurons (Fig. 2A–C). Voltage-gated Na$^+$ and K$^+$ currents in CLT L124W neurons were smaller than those currents in CLT WT neurons (Fig. 2D). However, CLT L124W did not display deficiency in firing action potentials (Fig. 2E). Next, when examining
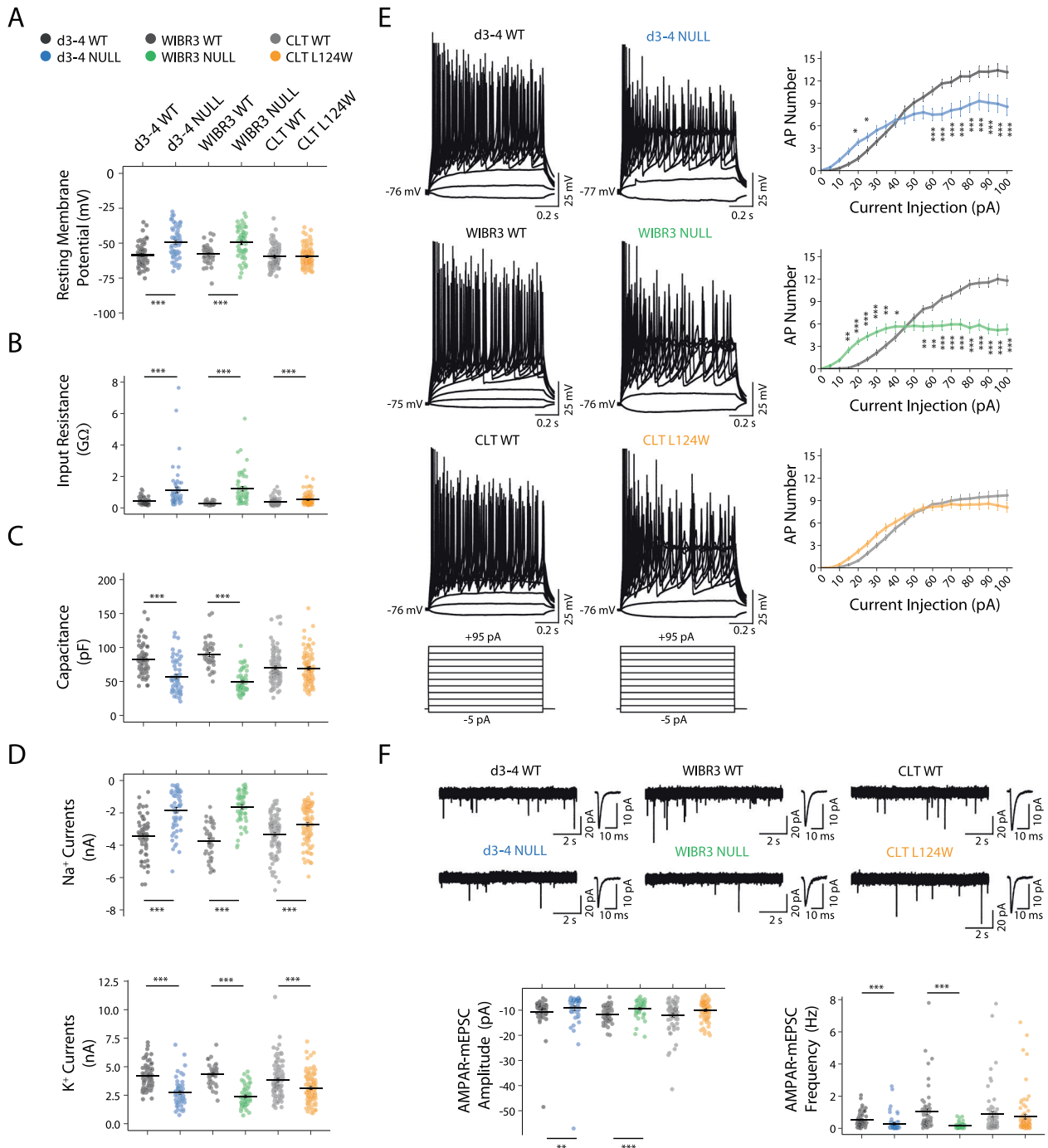
Fig. 2 **Deficits in intrinsic membrane properties and excitatory synaptic function in RTT neurons. A–D** Scatter plots showing all data points for the resting membrane potentials (**A**), input resistance (**B**), cell capacitance (**C**), voltage-gated Na$^+$ currents measured at -10 mV (**D**, Top), and voltage-gated K$^+$ currents measured at $+60$ mV (**D**, Bottom) in 4–5 week-old *Ngn2* neurons of WT ($n = 66$, 42, and 99, respectively) and RTT from d3-4 ($n = 58$), WIBR3 ($n = 55$), CLT ($n = 100$). The graphs also display average resting membrane potentials, input resistance, cell capacitance, Na$^+$ currents and K$^+$ currents. **E** Left, Representative traces showing evoked action potentials in 4–5 week-old *Ngn2* neurons of WT and RTT from d3-4, WIBR3 and CLT. Right, Plots depict the numbers of evoked action potentials triggered by a series of current steps from $+5$ pA to $+100$ pA for 1 s in 4–5 week-old *Ngn2* neurons of WT ($n = 66$, 42, and 99, respectively) and RTT from d3-4 ($n = 58$), WIBR3 ($n = 55$), CLT ($n = 100$). **F** Top, Typical traces display mEPSCs in 6 weeks old *Ngn2* neurons of WT and RTT from d3-4, WIBR3 and CLT. Inset shows averaged mEPSCs in the neuron on the left. Bottom, Scatter plots display all data points for the amplitude and frequency of mEPSCs. The graphs also display average amplitude and frequency of mEPSCs in 6 weeks old *Ngn2* neurons of WT ($n = 56$, 58, and 68, respectively) and RTT from d3-4 ($n = 62$), WIBR3 ($n = 44$) and CLT ($n = 78$). All data were shown as mean $+/-$ SEM. 2 lines of isogenic WT and 2 lines of CLT L124W data were pooled. Statistical significance was evaluated by Student's *t*-test or Mann–Whitney test, as appropriate, in Panel (**A–D** and **F**), and by two-way repeated measure ANOVA followed by post hoc test in Panel (**E**). *$p < 0.05$, **$p < 0.01$, ***$p < 0.001$.

excitatory neurotransmission in CLT WT neurons and CLT L124W *Ngn2* neurons, neither AMPAR-mEPSC amplitude nor frequency in CLT L124W neurons were different from CLT WT neurons (Fig. 2F). Therefore, recordings from CLT WT and CLT L124W *Ngn2* neurons show increased input resistance and impaired voltage-gated Na$^+$ and K$^+$ currents in the mutant neurons. Greater magnitude increases in input resistance and impairment of Na$^+$ and K$^+$ currents were also observed in *MECP2* null neurons. In addition to this core subset of phenotypes shared with CLT L124W neurons, *MECP2* null neurons showed differences, in comparison with their isogenic controls, in resting membrane potentials, cell capacitance, action potential firing, and excitatory synaptic function.

Altered neuronal size, complexity and excitatory synapse density in RTT *Ngn2* neurons

Reduced size and complexity have been identified as prominent morphometric features of classic RTT using human NPC-derived cortical neurons [10, 13, 14]. To assess morphometry in *Ngn2* neurons, 6 week old neuron co-cultures with mouse astrocytes were sparsely labelled with GFP in 3–5 independent experiments. Fixed cells were stained for DAPI, GFP and MAP2, and images captured on a confocal microscope reveal similar cell densities for all genotypes (Fig. 3A). Soma area and dendrite tracing was performed by two observers blinded to genotype. As anticipated, *MECP2* null (d3-4, WIBR3 and PGPC14) neurons had decreased average soma area and total dendrite length, recapitulating the known classic RTT-associated phenotypes that are implicated in microcephaly (Fig. 3B, C). In contrast, the CLT L124W missense neurons exhibited no changes in soma area or dendrite length (Fig. 3B, C), consistent with the normal head circumference of preserved speech variant atypical RTT and with our finding that capacitance is not changed.

However, Sholl analysis of the CLT L124W neurons revealed decreased branching complexity relative to WT, similar to the reduced branching complexity in *MECP2* null neurons relative to WT (Figs. 3D & S3A). To investigate changes in synapses, excitatory synapse density was quantified based on co-localization of pre-synaptic SYN1 and post-synaptic HOMER1 puncta along dendritic MAP2 signal. The d3-4, WIBR3 and PGPC14 *MECP2* null neurons showed reduced SYN1/HOMER1 density compared to its respective isogenic control. On the other hand, CLT L124W neurons did not show significant changes relative to WT (Fig. 3E). Taken together, CLT L124W neurons show only the core subset of dendrite complexity changes shared with *MECP2* null neurons, consistent with more limited mutation-dependent phenotypes found in L124W protein heterochromatin association and excitatory neuron activity.

Aberrant network circuitry in RTT *Ngn2* neuronal cultures

During development, individual neurons connect to one another forming neuronal networks that produce distinctive patterns of synchronized activity. Such patterns play a critical role in shaping the network structure and function in the developing brain [42]. Upon observing alterations in functional and morphometric properties on the level of individual neurons, we determined if integrated neural circuit activity would be perturbed in RTT cultures. Isogenic WT and RTT *Ngn2* neurons (WIBR3, PGPC14 and CLT-L124W) were co-cultured with mouse astrocytes on 12-well MEA plates with 64 channels in an 8 × 8 grid per well (Axion Biosystems) (Fig. S4A). Every plate was derived from an independent differentiation from *Ngn2*-inducible iPSCs/ESCs and contained 3–6 wells of each isogenic genotype as technical replicates. Time zero was the day when neurons and astrocytes were plated together in co-culture, and five minutes of extracellular recordings were collected each week from week 3 through week 7.

We observed the emergence over time of high frequency neural activity in multiple electrodes similar to those observed in

previous experiments [21]. Raster plots of action potentials detected using Axion software show synchronous bursts across multiple electrodes for the WIBR3, PGPC14 and CLT isogenic pairs (Fig. 4A). As anticipated, we detected variability of firing regimes across the different WT lines (Fig. 4A) despite equivalent cell densities on the electrodes (Fig. S4A). This is consistent with a published guideline that reports variability across 10 different control lines and stresses the importance of using isogenic controls for assessing disease-associated phenotypic changes in human stem cell derived neural networks [35]. The number of electrodes with active signals increased over the time course of the recordings likely as a result of development of new connections within the network, but there was plate-to-plate variability in numbers of active electrodes (Fig. S4B). MEA plates were analyzed if at least one line on them had wells that reached a cut-off of at least 32 out of 64 electrodes active over the time course to reduce variability. With this cut-off, we could include plates that developed strong network activity and exclude ones with poor cell adherence. Additionally, at the final time point neurons were treated with the AMPAR antagonist CNXQ to show that spiking activity was abolished (Fig. S4C). This supported that synaptic transmission was responsible for network activity patterns.

Based on the mild electrophysiological and morphological differences in CLT L124W neurons, we predicted a similarly small change in variables that measure network activity. To account for differences in maturation dynamics between plates [21] we normalized the fold-change of RTT values to the respective WT isogenic values within a plate. We examined 6 biological replicate plates of CLT isogenic neurons, each with 3 wells of the four CLT lines. Cumulatively, the CLT L124W *Ngn2* neurons did not show significant differences in weighted mean firing rate (defined as the mean firing rate across active electrodes normalized to the number of active electrodes per well) relative to WT (Fig. 4B, right). At late timepoints, increased network burst frequency and decreased network burst duration were observed (Fig. 4C, D, right). Absolute values for the above network metrics are shown in Fig. S4B–D, and no other differences were observed in interburst interval, synchrony or other metrics.

To detect circuitry defects in *MECP2* null neurons, we then examined 6 biological replicate MEA plates of WIBR3 and 4 biological replicate MEA plates of PGPC14 isogenic pairs, each with 6 wells of isogenic WT and nulls. The RTT values are shown as relative log fold change compared to the WT baseline (normalized WT level indicated by dashed horizontal line). The weighted mean firing rate did not have a consistent change in *MECP2* null neurons relative to WT (Figs. 4B and S4D). However, the *MECP2* null network bursts showed a consistent decrease in frequency relative to WT beginning at the 4 week time-point (Figs. 4C and S4E). These decreased network burst frequencies were followed by longer network burst durations that transiently emerged at weeks 5–6 in WIBR3 and PGPC14 isogenic lines (Figs. 4D & S4F). The WIBR3 null isogenic lines had larger fold changes in network bursting properties compared to the PGPC14 null isogenic lines. In contrast, CLT L124W had only late time points with increased network burst frequency or decreased network burst duration that were distinct relative to those shown by *MECP2* null networks.

Modeling changes in peak bursting frequency in RTT *Ngn2* neural networks

Variations in the frequency of network bursts capture differences between RTT and WT, particularly for the *MECP2* null phenotypes showing more pronounced changes in cellular and network profiles. In order to better characterize such changes in the frequency domain and search for more subtle differences between the different network phenotypes we extracted raw spiking data and performed power spectral density (PSD) estimations on spike trains from each electrode within a well.
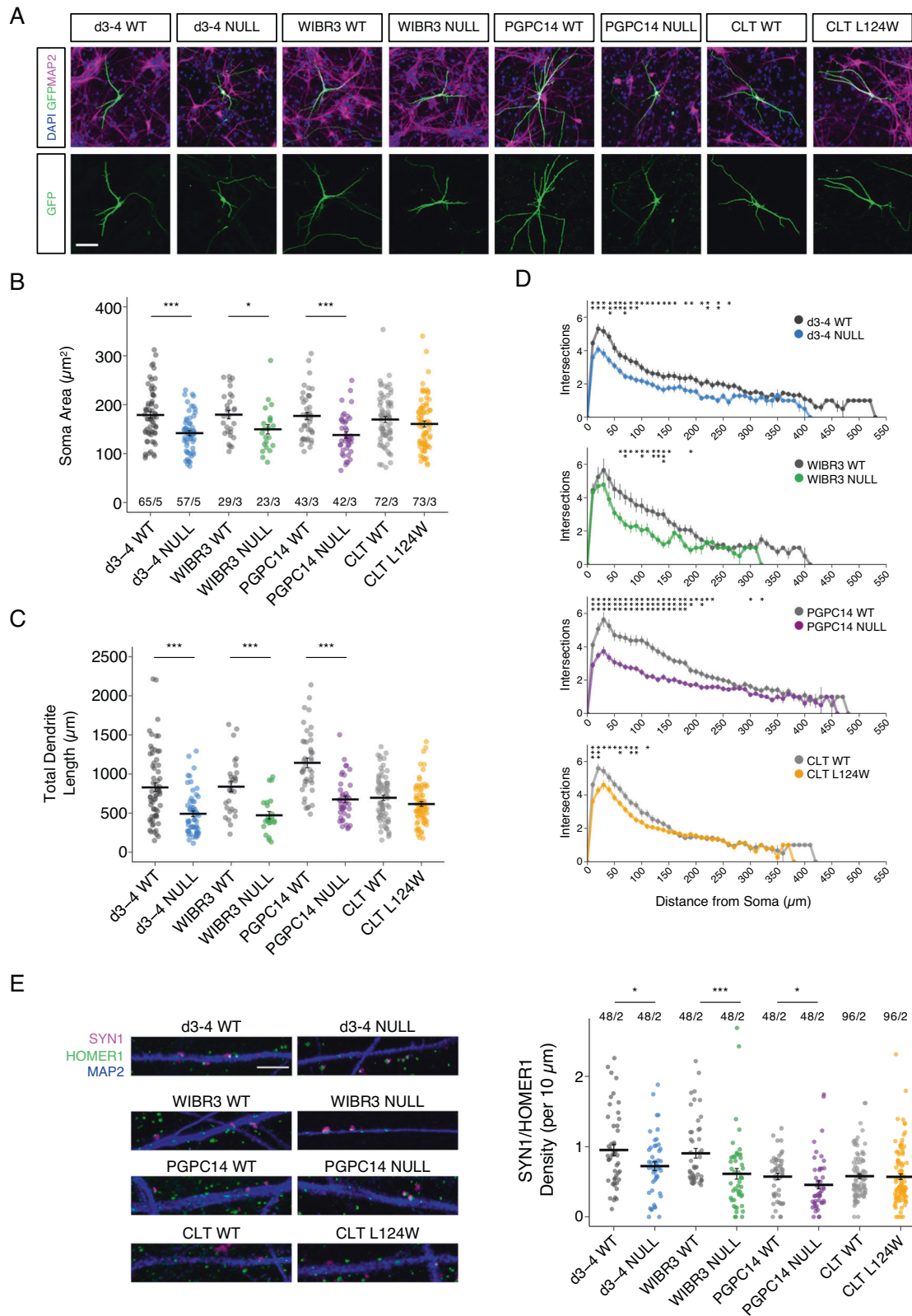
The PSD calculated directly on recorded spike trains in all 64 channels exhibits clear peaks shown in heatmaps of the frequency of these synchronous network bursts (Fig. 5A). When the distributions of peak bursting frequencies were aggregated from weeks 2–7 (Figs. 5B and S5A) or normalized to their respective isogenic control (Fig. 5C), the WIBR3 and PGPC14 nulls were reduced in cumulative median peak bursting frequency across all timepoints. The peak bursting frequency of CLT L124W was slightly increased. Our PSD estimates consistently distinguished *MECP2* null from WT *Ngn2* neural networks, and captured the

Fig. 3 RTT *Ngn2*-derived neurons have reduced size and complexity. A Representative images of 6 week old WT and RTT *Ngn2* neurons co-cultured with mouse astrocytes, with a GFP sparse labelling (green), pan-neuronal marker MAP2 (magenta) and DAPI (blue). Scale bar = 100 μm. **B** Neurons quantified for soma area, (**C**) Total dendrite length, and (**D**) Sholl complexity of individual neurons (10 μm increments from the soma). **E** Representative images of 6 week old WT and RTT *Ngn2* neurons co-cultured with mouse astrocytes, labelled with pre- and post- synaptic markers SYN1 (magenta) and HOMER1 (green), quantified for synapse density along dendrites labelled by MAP2 (blue). Scale bar = 5 μm. All data were shown as mean +/− SEM in Fig. (**B**–**D**). Indicated are n/N = total number of neurons/number of replicate batches (4–6 wells of each cell line per batch), and in Fig. (**E**) n/N = total number of dendrite segments/number of replicate batches (4 wells of each cell line per batch). 2 lines of isogenic WT and 2 lines of CLT L124W data were pooled. Statistical significance was evaluated by Student's *t*-test or Mann Whitney test, as appropriate, in Panel (**B**–**E**). *$p < 0.05$, **$p < 0.001$, ***$p < 0.001$.
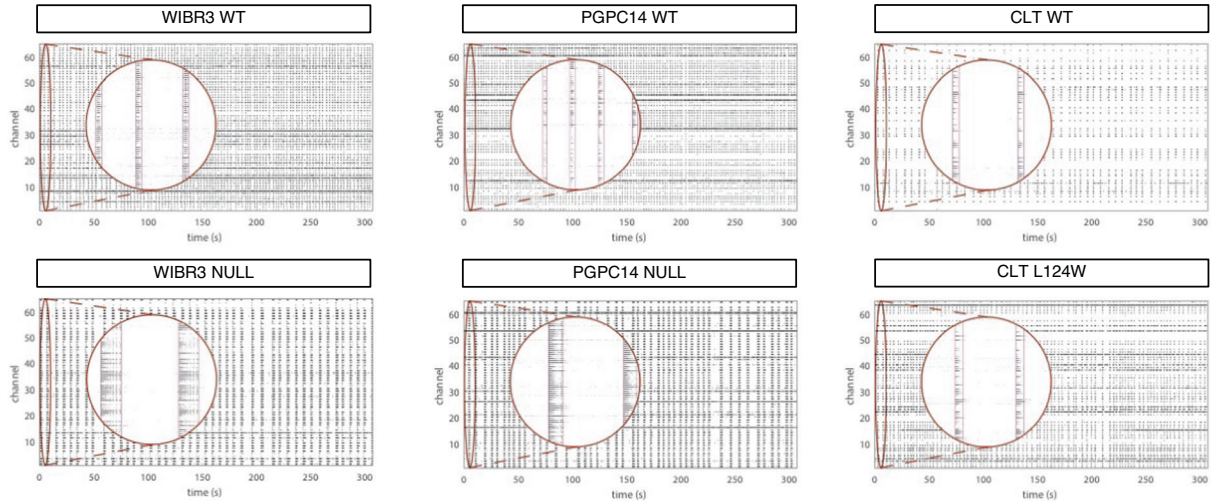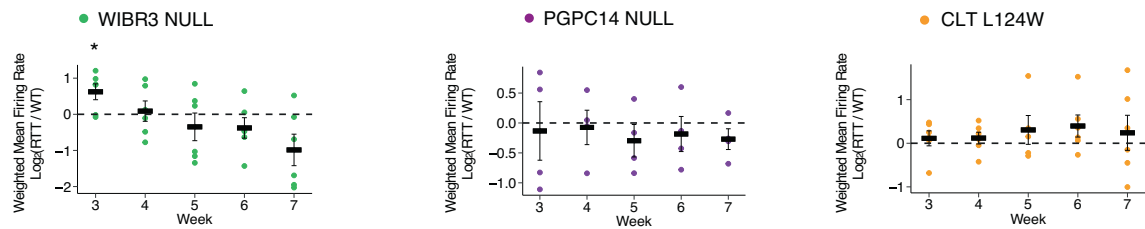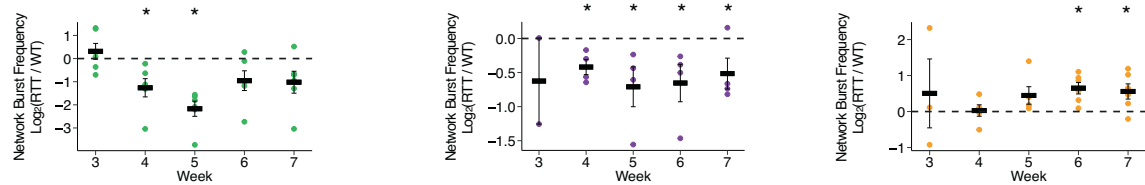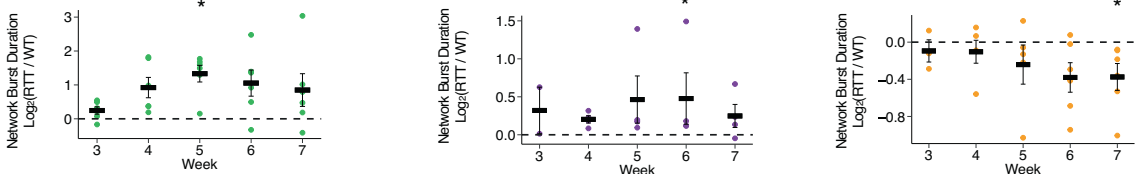

Fig. 4 *MECP2* null *Ngn2* neurons exhibit altered network bursting activity. A Representative 300 s MEA raster plots of spontaneous action potential spikes (black lines) from WT and RTT *Ngn2* neurons co-cultured on mouse astrocytes at 5 weeks, detected across grid of 64 electrode channels. Inset (circular window) is a magnification of the selected region, showing spikes across multiple channels within synchronous network bursting events. **B** Quantification of MEA activity shown as log fold change of RTT relative to WT for weighted mean firing rate, (**C**) network burst frequency, and (**D**) network burst duration. 6 replicate plates of WIBR3, 4 replicate plates of PGPC14 and 6 replicate plates of CLT isogenic pairs, with 2–6 active wells analyzed per genotype per plate. All data were shown as mean +/− SEM, *$p < 0.05$. 2 lines of isogenic WT and 2 lines of CLT L124W data were pooled. Statistical significance was evaluated by Student's *t*-test or Mann–Whitney test, as appropriate, in Panel (**B**–**D**). *$p < 0.05$.
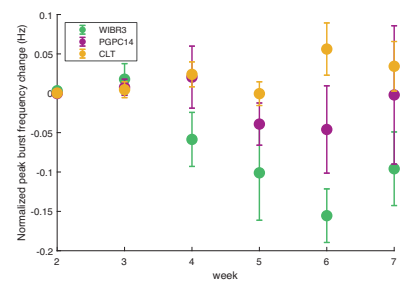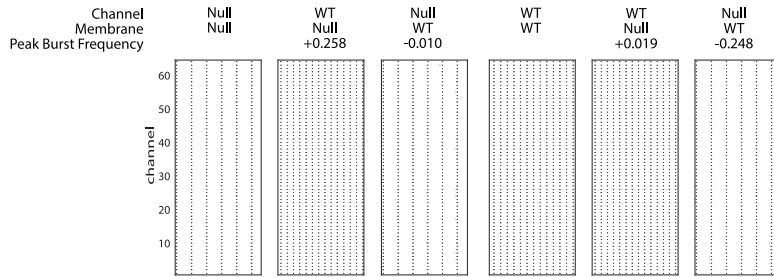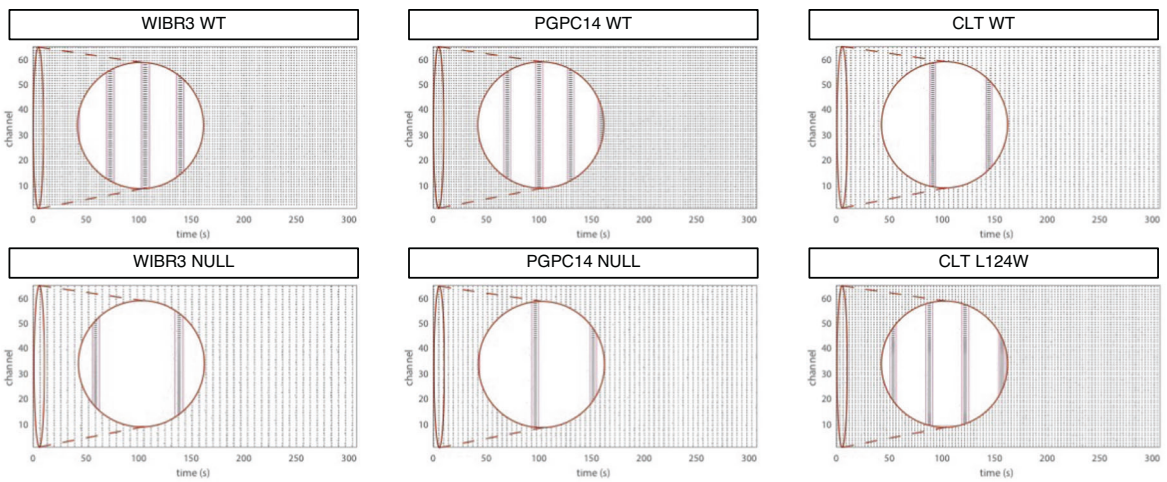
A
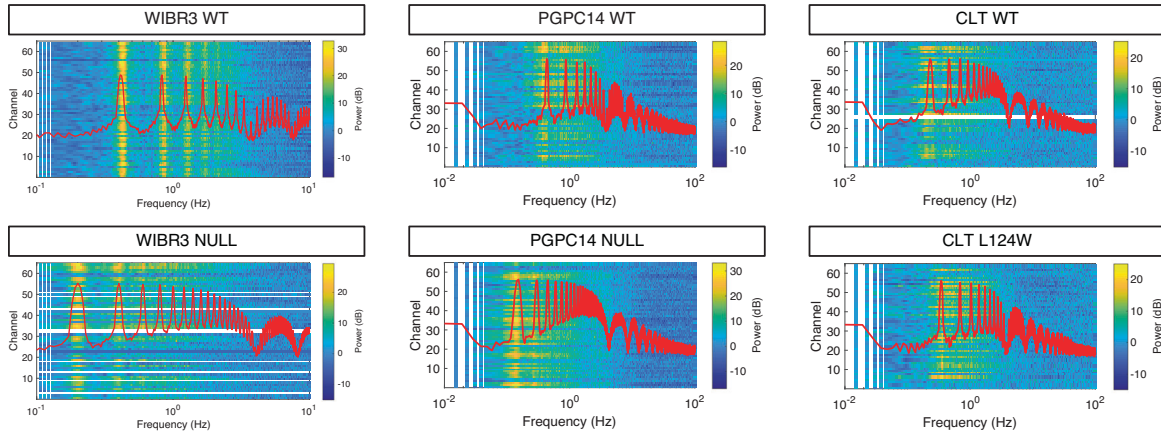
B
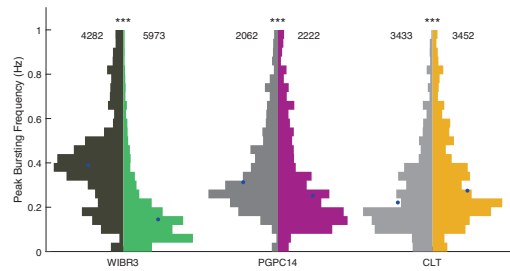
C

D

E

difference between the *direction* of peak burst frequency change in the CLT L124W compared to *MECP2* null neurons.

Changes in burst frequency can have at least two different origins, one is changes in the intrinsic properties of individual neurons, and the second is changes in network synaptic connectivity. First, to test whether the observed differences in peak burst frequency in RTT networks were based on changes to altered intrinsic properties (for example voltage-gated Na^+ and K^+ currents, capacitance or resting membrane potentials) we developed a computational model of excitatory spiking neurons

Fig. 5 RTT *Ngn2* neurons display changes in bursting dynamics. A Power spectra of spike trains from recorded WT and RTT *Ngn2* neurons (heatmap), along with the average power spectrum across 1000 simulated neurons in the spiking network model (red line). Peaks in the experimental data (heatmap) and the computational model (red lines) match well. **B** Peak bursting frequency distribution aggregated from MEA recordings of WT and RTT *Ngn2* neurons from weeks 2–7. 6 replicate plates of WIBR3, 4 replicate plates of PGPC14, and 5 replicate plates of CLT, with 3–6 active wells analyzed per genotype per plate. The CLT plate 17 was excluded because of inadequate network bursts in weeks 2–5 and lower numbers of active wells (2–3 per genotype). Indicated are number of electrodes analyzed, blue dot represents median. Statistical significance was evaluated by Mann Whitney test. ***$p < 0.001$. **C** Normalized change in peak frequency from WIBR3 NULL, PGPC14 NULL and CLT L124W *Ngn2* neurons across weeks 2–7 shows a developmental trajectory and clear differences between mutant subtypes. **D** Computational drop-out experiment to understand how Na$^+$ and K$^+$ channel values vs. capacitance, resting membrane potential values contribute to the frequency changes. Change is relative to WIBR3 Null (with respective Null channel, capacitance, and resting membrane potential values) and WIBR3 WT (with respective WT channel, capacitance, and resting membrane potential values). **E** Example 300 s raster plots generated by the computational modelling approach for WT and RTT genotypes across 64 channels. The *x* axis is time, the *y* axis is electrode number and the black lines are multiunits events (cluster of action potentials) at each channel. Inset (circular window) is a magnification of the selected region.

connected into a network that approximates the iPSC-derived cultures. A network of 1000 excitatory adaptive integrate-and-fire (AdIF) neurons [43, 44] was simulated using parameters derived from the patch-clamp recordings. We modelled random intra-network connections, connection probability of 0.05 (resulting in an average of 50 synapses per cell), and random Poisson external input (100 synapses spiking at 20 Hz). This spiking model displayed robust network bursts, the features of which are related to single-neuron properties in the network. We then analyzed simulated spike trains in the same way as the experimental data. Overlay of the peak frequency derived from the top fit AdIF simulations (red line in Fig. 5A) demonstrated that this spike *adaptation*-driven model recapitulated the reduced frequency observed in the WIBR3 and PGPC14 null neuron recordings. Strikingly, the AdIF simulations also captured the effect in the opposite direction for the CLT L124W neurons where the network peak frequency was increased. This model demonstrates that changes in Na$^+$ and K$^+$ currents, capacitance or resting membrane potential, or combinations of them, are sufficient to account for the network peak burst frequency differences.

Next, we addressed whether systematic differences in network/synaptic connectivity between RTT and WT networks could cause the observed differences in burst frequency. To this end we studied the WIBR3 network model over a range of subthreshold adaptation values (4 to 10 nS) and connection probabilities (0.05 to 0.35). Over this range, network burst frequency increases with the decreased connection probability typically observed in RTT neuron networks [45], while the value of subthreshold adaptation has a smaller effect (Fig. S5B). The effect of connection probability on burst frequency is opposite to that observed in the experimental data, indicating that changes in synaptic connection probability do not explain our observations. This control simulation is consistent with intrinsic adaptation currents driving the observed changes in burst frequency.

Finally, to determine the contributions of Na$^+$ and K$^+$ currents relative to membrane capacitance and resting potential properties in driving peak burst frequency patterns in RTT, we performed drop out simulations by replacing the WIBR3 null values with their isogenic WT values. As shown in Fig. 5D, simulation with the null values gives a low frequency of bursts over the representative 30 s duration. When the null Na$^+$ and K$^+$ channel values, represented by the adaptation currents, are dropped out and replaced by the WT values, the simulation predicts that burst frequency is rescued. In contrast, when the null membrane values (capacitance and resting membrane potential) are dropped out and replaced by the WT values, there is no substantial change to the frequency. Reciprocal simulations where the WT values are dropped out and replaced by the null values also predict that it is only the null Na$^+$ and K$^+$ channel currents that drive the slow bursting frequency. The simulation model over 300 s durations (Fig. 5E) agrees with the experimental circuitry findings for both the *MECP2* null and CLT L124W neurons, and indicates that the *MECP2* null burst frequencies

are driven by experimentally validated changes in Na$^+$ and K$^+$ currents.

DISCUSSION
In this study, we defined a wide phenotypic spectrum of *MECP2* mutation-dependent changes in heterochromatin binding, neuron morphology, electrophysiological properties and network connectivity by modeling atypical and classic RTT neurons in vitro. We investigated the effects of a novel *MECP2* L124W MBD atypical variant in comparison with three classic *MECP2* nulls in isogenic induced excitatory neurons. Our findings uncover core functional and morphological phenotypes present in both types, and a broader set of additional impairments exhibited by null neurons (summarized in Table 1). The core phenotypes present in atypical RTT included increased input resistance, impaired voltage-gated Na$^+$ and K$^+$ currents, and reduced dendritic complexity. *MECP2* null neurons consistently displayed the same core phenotypes as well as depolarized resting membrane potential, reduced cell capacitance accompanied by decreased soma area, dendrite length and excitatory synapse density, and had disruptions in excitatory synaptic transmission. Both the L124W and null neurons exhibited a shared core phenotype in neuronal network burst frequency and duration patterns but these changed in opposite directions. Simulation modeling using parameters derived from the patch-clamp recordings replicated the increased network burst frequency in L124W and the decreased frequency in null neurons. Drop out simulations on the null neurons predicted that network burst frequency changes were driven by Na$^+$ and K$^+$ channel currents. Thus, the *MECP2* null phenotypic profile encompassed known RTT-associated changes that validated our induced neuron model and revealed novel insights into the development of excitatory synaptic activity and network circuitry.

L124W molecular, cellular and network core phenotypes
The atypical RTT-associated phenotypic profile of L124W MECP2 protein was supported by evidence of partially disrupted chromocenter binding in mouse cells and stable unchanged protein level in induced neurons. The chromocenter assay was recently used to demonstrate that MECP2 is a component of heterochromatin condensates that are predicted to play a role in disease pathways in RTT, and that MBD missense mutations often compromise this activity [8]. This mechanism likely alters the set of genes repressed by L124W MECP2 in neurons. One potential experimental artefact we excluded was XCI erosion in the CLT L124W iPSCs. Since expression of the Xi was not reactivated, no WT MECP2 was produced in neurons to rescue L124W phenotypes. Overall, the L124W variant represents a subtype of MECP2 MBD mutation that retains partial function in contrast to the more disrupted heterochromatin found in previous studies of L124F, R106W and other MBD missense variants [7].

Table 1. Summary of identified RTT *Ngn2* neuronal phenotypes.

	Cell Line/*MECP2* Mutation			
	d3-4 Null	WIBR3 Null	PGPC14 Null	CLT L124W
DNA Binding				
Chromocenters				Disrupted
FRAP				↑ Recovery
Intrinsic Electrophysiological Properties				
Resting membrane potential	↑	↑		No change
Input resistance	↑	↑		↑
Cell capacitance	↓	↓		No change
Evoked AP number*	↓	↓		No change
Na$^+$/K$^+$ currents	↓	↓		↓
AP amplitude	No change	No change		No change
AP threshold	No change	↑		No change
AP rise time	↑	No change		No change
AP D$_{1/2}$	No change	No change		No change
AP decay	No change	No change		No change
Synaptic Function				
mEPSC amplitude	↓	↓		No change
mEPSC frequency	↓	↓		No change
Morphology				
Soma area	↓	↓	↓	No change
Dendrite length	↓	↓	↓	No change
Complexity	↓	↓	↓	↓
Excitatory synapse density	↓	↓	↓	No change
Network Circuitry				
Weighted mean firing rate		No change	No change	No change
Network burst frequency		↓	↓	↑
Network burst duration		↑	↑	↓

Core phenotypes altered in all lines highlighted in gray.
*When current step injection (over +60 pA).

We found that CLT L124W neurons showed core phenotype changes in dendrite complexity and intrinsic properties similar to the WT. Importantly, CLT L124W neurons showed increased input resistance. As a consequence of higher input resistance a given depolarizing current will produce a larger change in membrane potential. Thus, increased input resistance explains our finding that the amount of depolarizing current required to evoke an action potential was lower in all mutants as compared with their corresponding controls (Fig. 2E). From this result we conclude that RTT neurons have increased excitability because they have a greater chance to trigger an action potential with a given depolarizing current. A recent study on R106W missense iPSC derived neurons also found a graded response in some morphological features and electrophysiological properties compared to MECP2 knockdown neurons, and did not detect changes in synaptic function that were evident in knockdown neurons [46]. In our case we also examined Na$^+$ and K$^+$ currents in CLT L124W and *MECP2* null neurons, and found these currents are consistently decreased relative to those in WT. As we found limitation of sustained firing of action potentials in response to prolonged current injection in mutant neurons, as compared to WT, we conclude that the decrease in Na$^+$ currents predominates over the decrease in K$^+$ currents (Fig. 2E). In addition, our network circuitry studies using MEA revealed a core phenotype that network burst frequency and duration are changed, and the opposite direction of this change in CLT L124W and *MECP2* null neurons was successfully modelled computationally.

A potential role for modifier genes that mitigate the cellular and network phenotypes in the atypical RTT neurons could be examined in future by whole genome sequencing for known variants, and by generating a null mutation in the active *MECP2* allele of the CLT L124W iPSC lines to test if their phenotype is milder than the consistent phenotype observed in the three *MECP2* null mutants. We also recognize the possibility that L124W may have functional effects on other cell types. For example, RTT astrocytes have been shown to exert non-cell autonomous effects

on WT and mutant neurons [47, 48]. As inhibition was absent in our excitatory neuron model, co-culturing CLT L124W astrocytes with glutamatergic and GABAergic neurons in monolayers or organoids could explore the potential interplay of these signals in single neurons and network activity [49–51].

MECP2 null full phenotype and modeling of RTT networks
The *MECP2* null full phenotype included smaller soma size and dendrite length, reduced synapse numbers, and reduced AMPAR-mEPSC amplitude and frequency. Importantly, we observed robust network bursting phenotypes in *MECP2* null neurons. The multi-unit spiking pattern changes revealed that network-wide events occurred less frequently and had extended burst trains in *MECP2* nulls compared to WT. In molecular terms, when there is complete loss of MECP2 protein all interactions of cofactors with any MECP2 domain would be abrogated. The outcome would be expected to impact transcription of every gene that is directly regulated by MECP2 binding, and there may be additional impacts on miRNA processing that would affect mRNA stability, splicing to generate alternative isoforms, and strong reductions in protein translation. These latter pathways, in combination with the more severe effects on direct transcription targets, could have complex outcomes in circuits that differ in direction from those in L124W neurons.

The *MECP2* null circuitry phenotype shows similarity to the reduced rate and increased duration of network bursts observed in Kleefstra syndrome induced excitatory neural cultures cocultured with rodent astrocytes, where these changes were found to be mediated by upregulation of *N*-methyl-D-aspartate receptor subunit *GRIN1* expression [22]. Highly perturbed RTT-associated oscillatory network activity phenotype in local field potential MEA recordings of isogenic WT and *MECP2* knockout iPSC-derived cortical organoids showed complete absence of network events [50].

A possible explanation for changes in network dynamics are changes in the intrinsic properties of neurons that may impact their ability to generate bursting patterns. Our spiking network model examined this issue. Model simulations indicate that the changes in RTT null networks bursting frequency may be mediated by neuronal adaptation currents such as inactivation of depolarizing Na^+ currents, and activity dependent (i.e. calcium dependent) activation of slow hyperpolarizing K^+ channels [43, 52], which may be downstream targets of MECP2 [15, 53]. This is supported by the decrease in K^+ currents seen in RTT neurons (Fig. 2). We have also previously found that *MECP2* null neurons derived from NPCs have altered protein levels of K^+ channels and AMPA receptors [54]. Finally, the computational drop-out simulations support the hypothesis that changes in intrinsic Na^+ and K^+ currents are the driving variable of the observed changes in burst frequency. Because these currents are known to be critical in shaping neuronal excitability, gain, and responses to sensory input, these changes could play important roles in cortical function [44, 55].

Significance
In summary, we used a multilevel approach to identify a range of RTT-associated phenotypes relating to form and function in isogenic human stem cell-derived excitatory neurons harbouring a novel L124W missense or *MECP2* null mutations. We demonstrate a mild heterochromatin association phenotype in L124W MECP2 that is mutated in an atypical RTT patient with the preserved speech variant. We define a core set of cellular and network phenotypes in atypical RTT neurons, and identify additional synaptic and morphological phenotypes present in null neurons. Network burst frequency and duration changes were observed but in opposite directions for atypical and null neurons. Our simulations demonstrate the utility of spiking models for analyzing changes in stem cell-derived RTT neuron networks and these simulations can be applied to the study of other neuropsychiatric disease states. The striking network burst frequency changes revealed in *MECP2* null neurons provide a

potentially screenable phenotype for testing candidate compounds to rescue the RTT-associated changes in this in vitro assay to moderate disease. Full rescue might require correction of protein translation regulation and thus of the Na^+ and K^+ channel current deficits found in the core phenotypes.

METHODS
Protein model, chromocenter and FRAP assays
Human MECP2-MBD crystallographic structure was illustrated using PyMol Molecular Graphic System (PDB accession code: 3C2I), showing MBD bound at methylated double stranded DNA sequence of *BDNF* promoter, with point mutation location indicated. All imaging and image analysis for chromocenters were performed as previously described [32, 56] using the Fiji Particle Analysis plugin. FRAP Time-lapse imaging was carried out as a series of confocal time lapse images of frames (512×512 pixels) imaged at 488 nm laser excitation with 0.05 transmission were used to record GFP-tagged protein post bleach recovery. FRAP assay was recorded with a minimum of nine pre-bleach frames, one frame after $1000\,\mu s$ bleaching with 405 nm laser line at 100% transmission, and 90 post-bleach frames were recorded at equal time intervals.

Ethics and iPSC reprogramming
iPSCs were reprogrammed under approval of the Canadian Institutes of Health Research Stem Cell Oversight Committee and the Research Ethics Board of The Hospital for Sick Children (REB #1000050639) and the University of California San Diego (IRB #14123ZF). Existing iPSC lines are listed in Table S1.

CLT iPSC lines were generated from fibroblasts after informed consent was obtained. Fibroblasts were collected from a small incision in the skin after a skin biopsy and tissue was washed in PBS 1x with 4% penicillin/streptomycin (Gibco). Later, the tissue was broken into small pieces using needles and plated in culture media (DMEM/F12, 15% FBS, 1% MEM NEAA, 1% L-glutamine and 1% penicillin/streptomycin). After 1 month, fibroblasts migrated out from the tissue. After reaching high confluency, cells were expanded or frozen as stock [57, 58]. Fibroblasts were reprogrammed using Sendai virus (Invitrogen) in feeder-free conditions on Matrigel (Corning) with mTeSR1 (STEMCELL Technologies). After colonies started to grow, colonies were picked manually and expanded on feeder-free Matrigel-coated dishes and frozen with CryoStore (STEMCELL Technologies). Mycoplasma contamination was routinely checked.

iPSC/ESC culturing and maintenance
Human iPSC/ESCs (Table S1) were maintained on dishes coated with Matrigel in mTeSR1 or StemMACS iPS-Brew XF (Miltenyi Biotec) media with 1% penicillin/streptomycin. iPSCs were passaged weekly with ReLeSR (STEMCELL Technologies) with daily media changes except for the day following passaging. Accutase (Innovative Cell Technologies) and media with 10 µM Rho-associated kinase (ROCK) inhibitor (Y-27632, STEMCELL Technologies) was used for any single-cell dissociation. Routine mycoplasma testing was performed.

Karyotyping
iPSC karyotyping and standard G-banding chromosome analysis (400-banding resolution) was performed by The Centre for Applied Genomics (TCAG) at The Hospital for Sick Children.

Pluripotency assays
iPSC colonies were fixed and stained with pluripotency markers OCT4, NANOG, SSEA4 and TRA-1-60. Following embryoid body formation and spontaneous 3-germ layer differentiation for 16 days, resulting cells were fixed and stained for α-SMA, AFP and β-III-tubulin. To assess gene expression profile of iPSCs, RNA was extracted from 1 confluent well of a 6-well plate using RNA PureLink RNA mini kit (Life Technologies) as per manufacturer's protocol. Samples were sent to TCAG at the Hospital for Sick Children for Bioanalyzer assessment and sequenced as paired end 2×125 bases on an Illumina HiSeq 2500 at a depth of 15 M reads. Resulting FASTQ files were uploaded to www.pluritest.org for analysis [37]. Files can be found with GEO accession GSE148435.

XCI assays
Androgen receptor (AR) assay was performed as previously described [10]. In brief, 400 ng of genomic DNA from iPSCs/ESCs was digested by CpG

methylation-sensitive restriction enzymes *Hpa*II and *Hha*I for 6 h. 2 µL of digestion was amplified using Platinum Taq DNA Polymerase High Fidelity (Invitrogen) with AR gene primers with a FAM label (Table S2). Male samples were used as a control to confirm complete digestion. Electrophoresis was performed by TCAG at The Hospital for Sick Children. Traces were analyzed using PeakScanner (Thermo Fisher Scientific). To identify which *MECP2* allele was expressed on the active X chromosome, RNA was isolated from iPSCs and reverse transcribed into cDNA using SuperScript III (Invitrogen). Primers flanking the variant region (Table S2) were used for amplification with Platinum Taq DNA Polymerase High Fidelity or Q5 High Fidelity DNA Polymerase (New England BioLabs), followed by cloning as per the TOPO TA Cloning Kit (Invitrogen) or Zero Blunt TOPO Cloning Kit (Invitrogen) in OneShot TOP10 (Thermo Fisher Scientific) or Max Efficiency DH5α (Invitrogen) competent *E. coli* strains. 5–10 bacterial colonies per iPSC cell line tested were picked and grown in LB Medium (MP Biomedicals) for DNA extraction with Quick Plasmid MiniPrep Kit (Invitrogen). Samples were Sanger sequenced at TCAG and aligned to WT *MECP2* template using benchling.com.

CRISPR/Cas9 gene editing
The *MECP2* indel mutation was generated using a previously described gene editing strategy [36]. Briefly, pSpCas9(BB)−2A-Puro (PX459) V2.0 (Addgene #62988) was cloned with an oligonucleotide designed to target *MECP2* exon 3 using benchling.com CRISPR prediction tool (described in Table S2). Indels were introduced by transfecting 8×10^5 cells with 1.5 µg plasmid in 100 µl scale using the Neon Transfection System (ThermoFisher) with one pulse at 1500 millivolts for 30 milliseconds (~40–70% transfection efficiency). Transfected cells were plated in 2 wells of a 6-well plate with mTeSR1 media supplemented with CloneR (STEMCELL Technologies) to enhance cell survival. From D2-5, puromycin (0.5 ug/ml) was added daily to mTeSR1 media changes and surviving single colonies were grown to D12-18 before transferring to 24-well plates. Isolated clones were passaged and gDNA was harvested with a Quick DNA miniprep kit (Zymo) and PCR products were sent for Sanger sequencing by TCAG at the Hospital for Sick Children.

Lentivirus generation and transduction
FUW-TetO-Ngn2-P2A-EGFP-T2A-puromycin and *FUW-rtTA* plasmids for excitatory cortical neuron differentiations were kindly gifted by T. Sudhof [40] and packaged as per a previously described protocol [59]. Lentiviruses were produced in HEK293T cells using a third generation packaging system (*pMDG.2*, *pRSV-Rev* and *pMDLg/pRRE*). Viral particles in the supernatant were collected 48 h post-transfection, filtered and concentrated by $91,000 \times g$ centrifugation for 2 h at 4 °C. For iPSC transductions, accutase (Innovative Cell Technologies) was used to obtain 5×10^5 cells single-cells per well of a Matrigel-coated 6-well plate that were incubated with concentrated virus in mTeSR1 with 10 µM ROCK inhibitor and 8 µg/ml polybrene (Sigma) for 8 h. Media was changed to mTeSR1 and transduced iPSCs were maintained and expanded to acquire frozen stocks.

Ngn2 neuronal direct conversion
Excitatory cortical neurons were generated as previously described [36, 39]. Briefly, on Day 0 iPSCs were made into single-cells by accutase and plated at 3×10^5–1×10^6 cells per well on Matrigel-coated 6-well plates with StemMACS iPS-Brew XF media supplemented with 10 µM ROCK inhibitor. All media mentioned for Day 1–8 contained 1x penicillin/streptomycin (Gibco), 1 µg/mL laminin (Sigma), 2 µg/mL doxycycline hyclate (Sigma), 10 ng/ml BDNF (Peprotech) and 10 ng/mL GDNF (Peprotech). On Day 1, media was changed to CM1 consisting of DMEM/F12 (Gibco), 1x N2 (Gibco) and 1x NEAA (Gibco), supplemented with 10 µM ROCK inhibitor. On Day 2, media was changed to CM1 supplemented with 2–5 µg/mL puromycin (Sigma). On Day 3, media was changed to CM2 consisting of Neurobasal (Gibco), 1x B27 (Gibco) and 1x Glutamax (Gibco), supplemented with 2–5 µg/mL puromycin. On Day 4–5, media was changed to CM2. On Day 6, media was changed to CM2 supplemented with 10 µM Ara-C (Sigma). On Day 8, doxycycline induction was withdrawn and neurons were re-seeded onto coverslips or wells coated with 0.1 mg/ml poly-L-ornithine (PLO) (Sigma) and 40 µg/ml laminin (Roche or Sigma) in CM2 with BDNF and GDNF and co-cultured with P1 mouse astrocytes with media changes every 3–4 days unless otherwise noted for downstream assays.

Protein quantification
Protein was extracted from neurons (not grown with mouse astrocytes) washed in ice-cold PBS using radioimmune precipitation assay (RIPA) buffer (25 mM Tris-HCl, pH 7.6, 150 mM NaCl, 1% Nonidet P-40, 1% sodium deoxycholate and 0.1% SDS). Equivalent protein masses were loaded into capillaries for detection using the 12−−230 kDa Separation Kit for the Wes (ProteinSimple). Multiplexed probing of MECP2 and β-actin by chemiluminescence was quantified using Compass for SW software (ProteinSimple).

Patch-clamp electrophysiology
Electrophysiological recordings were made as reported previously [11, 41]. Briefly, whole-cell patch-clamp recordings were performed with an Axopatch 1-D amplifier (Molecular Devices, USA) operated with Clampex 9.2 software and a DigiData 1200 series interface (Molecular Devices, USA), and the currents were sampled at 10 kHz and filtered at 2 kHz. The recordings were analyzed off-line using Clampfit 9.2 software (Molecular Devices, USA). All electrophysiological experiments and data analysis were conducted with *Ngn2* neuron samples blinded to the investigator. To examine intrinsic membrane properties, the recordings were performed in a 35-mm tissue culture dish filled with an extracellular solution containing (in mM): 140 NaCl, 5.4 KCl, 1 MgCl₂, 15 HEPES, 2 CaCl₂, 10 glucose, and the solution was adjusted to pH 7.35 with NaOH. Patch-clamp pipettes (5 to 8 MΩ) were pulled from capillary glass (1.5 mm diameter; World Precision Instruments, USA) using a P-87 pipette puller (Sutter Instrument Co., USA), and filled with an intracellular solution compose of (in mM): 144 K⁺-gluconate, 10 KCl, 2 Mg-ATP, 2 EGTA, 10 HEPES. The solution was adjusted to pH 7.2 with KOH. Voltage-gated ion currents, under the whole-cell voltage-clamp condition, were elicited at the holding membrane potential of −70 mV by stepping the membrane potential to a series of potentials from −80 mV to +60 mV for 400 ms. Action potentials, under current-clamp condition, were evoked from the membrane potential of around −75 mV by injecting a series of current steps from −5 pA to 100 pA (in 5 pA increments). Data from some neurons in both WT and mutant lines, with 10 pA increments, or maximum current injection of less than 100 pA, were pooled with those obtained with the current injection protocol above since there was no difference. In current-clamp, we subtracted a liquid junction potential of 16 mV from the membrane potential values measured with K⁺-gluconate based intracellular solutions.

To investigate synaptic function, mEPSCs, in voltage-clamp, were recorded in human *Ngn2* neurons at the holding membrane potential of −60 mV. Recording micropipettes were filled with an intracellular solution as described above. The extracellular recording solutions consisted of (in mM): 140 NaCl, 1 MgCl₂, 5.4 KCl, 1.3 CaCl₂, 25 glucose, 15 HEPES, 0.003 glycine, 0.001 strychnine, 0.01 bicuculline, 0.0005 tetrodotoxin, and pH was adjusted to 7.35 with NaOH. mEPSCs were detected and analyzed off-line using Mini Analysis Program (Synaptosoft Inc, USA).

Neuron sparse labeling
Neurons were transfected with *pL-SIN-EF1α-eGFP* plasmid (Addgene 21320) using 1 µg of DNA and 2 µL of Lipofectamine 2000 (Thermo Fisher Scientific) per well of a 24-well plate. 48 h post-transfection, neurons were fixed at 6 weeks and stained for MAP2 and GFP.

Immunocytochemistry and imaging
iPSCs were fixed with 4% formaldehyde in PBS for 8 min at room temperature. Neurons grown on 12 mm round glass coverslips (Bellco) or 24-well μ-Plates (Ibidi) were fixed with 4% formaldehyde in 0.4 M sucrose Krebs buffer for 8 min to preserve cytoskeletal integrity [60]. Fixed cells were permeabilized with 0.1% Triton X-100 for 8 min at room temperature and blocked for at least 1 h at room temperature in ICC buffer (10% normal goat (Cedarlane) or donkey (Sigma) serum in PBS with 0.05% Tween 20). Primary antibodies were diluted in ICC buffer and incubated overnight at 4 °C. Secondary antibodies were diluted in PBS with 0.05% Tween 20 and incubated for 1 h at room temperature. Unless otherwise indicated, nuclei were counterstained with 1 µg/ml DAPI in PBS for 5 min at room temperature. If cells were on coverslips, they were rinsed in molecular grade water and mounted on slides in Prolong Gold antifade mounting media (Thermo Fisher). Details for primary antibodies used in this study can be found in Table S3.

iPSC pluripotency and 3-germ layer assays were imaged with a Leica DM14000B epifluorescence microscope using a DFC7000T camera and LAS X software. Neurons for soma/dendrite tracing were imaged with an Olympus 1 × 81 spinning disk confocal microscope using a Hamamatsu C9100-13 EM-CDD camera and Volocity software (Perkin Elmer). Synapses were imaged with a Leica SP8 Lightning Confocal/Light Sheet point scanning confocal microscope and LAS X software.

Image analysis

Blinded images were analyzed using Filament Tracer in Imaris (Bitplane) by two individuals. Soma were manually traced with semi-automated reconstruction of dendrites on sparsely GFP labeled neurons that were co-stained with MAP2 (3–5 replicate batches, with 4–6 coverslips per cell line in a batch, total = 404 neurons). Synapse density was manually counted for over-lapping SYN1 and HOMER1 puncta along a given length of MAP2 dendrite signal (2 replicate batches, with 4 coverslips per cell line in a batch, total = 240 dendrite segments).

MEA plating and recording

12-well CytoView MEA plates (Axion Biosystems) with 64 channels per well in 8 × 8 electrode grids were coated with filter sterilized 0.1% poly(-ethylenimine) solution (Sigma) in borate buffer pH 8.4 for 1 h at room temperature, washed 4 times with water and dried overnight. Day 8 differentiated $Ngn2$ neurons were re-seeded at a density of 1×10^5 cells per 100 µL droplet in CM2 media consisting of BrainPhys (STEMCELL Technologies), 1x penicillin/streptomycin, 10 ng/ml BDNF and 10 ng/mL GDNF, supplemented with 400 µg/mL laminin and 10 µM ROCK inhibitor. Droplet of cells was applied directly on top of electrodes in each well, incubated for 1 h at 37 °C with hydration and then followed by slow addition of CM2 media supplemented with 10 µg/mL laminin. 24 h later, 2×10^4 P1 mouse astrocytes were seeded on top of the neurons in each well. CM2 media supplemented with 10 µg/mL laminin was changed consistently 24 h prior to recording twice per week from 2 weeks onwards on the Maestro MEA platform (Axion Biosystems). Each plate was incubated for 5 min on a 37 °C heated Maestro device, then recorded for 5 min of spontaneous neural activity using AxIS 2.0 software (Axion Biosystems) with a 0.2–3 kHz bandpass filter at 12.5 kHz sampling frequency. Spikes were detected at 6x the standard deviation of the noise on electrodes. Offline analysis used the Neural Metric Tool (Axion Biosystems), where an electrode was considered active if at least 5 spikes/min was detected. Poisson surprise burst and Envelope network burst algorithms with a threshold of at least 25% active electrode were applied. Further analyses and normalization of MEA metrics were completed in RStudio and MATLAB.

Statistical analyses

Statistical tests for assays were performed in RStudio (v1.1.423), SigmaPlot, GraphPad Prism, or MATLAB. D'Agostino & Pearson test was used to determine normality for datasets. Comparisons within respective isogenic pairs were conducted by two-way repeated measure ANOVA, Student's t, one sample t or Mann–Whitney tests where appropriate (*$p < 0.05$, **$p < 0.01$, ***$p < 0.001$).

Network model

The network model consists of N adaptive leaky integrate-and-fire (ADIF) neurons. Consistent with the biological iPSC-derived neuronal cultures studied here, the network is fully excitatory. The membrane potential V_i of the ith unit evolves in time according to the equations:

$$C_m \dot{V}_i = g_L(E_L - V_i) + g_e(E_e - V_i) - w$$

$$\tau_w \frac{dw}{dt} = a(V - E_L) - w$$

where C_m is the membrane capacitance, g_L is the leak conductance, E_L is the resting membrane potential, g_e is the time-dependent excitatory synaptic conductance, and E_e is the excitatory reversal potential. In the second equation, w is the adaptation variable, τ_w is the adaptation time constant, and a controls subthreshold adaptation.

When the membrane potential of neuron i exceeds threshold V_{th}, the neuron emits a spike, and the following reset conditions occur:

$$V_i \rightarrow V_r$$

$$g_e \rightarrow g_e + w_e \quad \forall j \in S$$

$$w \rightarrow w + b$$

where V_r is the reset potential, w_e is the excitatory synaptic weight, S is the set of neurons postsynaptic to neuron i, and b is the adaptation step current. Following the initial conductance increase caused by an incoming spike, the excitatory synaptic conductance follows simple exponential decay:

$$\tau_e \dot{g}_e = -g_e$$

where τ_e is the excitatory synaptic time constant. Populations of $N = 1000$ neurons were simulated for 300 seconds, representative of the in vitro culture recordings, with time-step of 0.1 ms in the Brian2 simulator [61]. Neurons were randomly connected with excitatory synapses and a connection probability of 0.05, leading to an average of 50 synapses per cell in the simulated networks.

Burst frequency

MEA raw voltage signals were measured for 300 s at a 12.5 kHz sampling frequency and Butterworth bandpass filtered between 200 Hz and 3000 Hz. Spike times were subsequently detected using an adaptive threshold crossing (threshold set at 6 × Std dev) and organized into spike trains per electrode, then further downsampled to 1 kHz. The power spectral density (PSD) of each spike train was estimated using MATLAB's pwelch() function, and was expressed in decibels (dB) as a ratio against the PSD of a randomly permuted version of the same spike train. The power spectrum provides a numerical weight for each measurable frequency of an input time series. The described synchronous, regular bursting corresponded to the global peaks of the spectra between 0 Hz and 1 Hz. Spectra with global peaks outside this range were found to not clearly exhibit such bursting and were therefore excluded from analysis.

Network scan

To identify the ideal time constant for adaptation (τ_w), we scanned a two-dimensional parameter space of capacitances (C_m) and neuronal membrane time constants (τ_m) in the range observed in patch-clamp recordings. Peak burst frequency in the simulations was evaluated through the same approach as the recorded culture data. Top simulations for the null and atypical CLT L124W conditions were determined as having the smallest absolute difference from the mean peak burst frequency of the recorded data.

To deconstruct the influence of various electrophysiologically-contributing variables to the changes in burst frequency, we performed a computational drop-out experiment. Here we changed either Na$^+$/K$^+$ currents or capacitance and resting membrane values, based on the reported values of the isogenic pair in Fig. 2, in the WIBR3 WT and WIBR3 null networks and calculated peak burst frequency as previously mentioned.

DATA AVAILABILITY

REFERENCES

1. Amir RE, Van den Veyver IB, Wan M, Tran CQ, Francke U, Zoghbi HY. Rett syndrome is caused by mutations in X-linked MECP2, encoding methyl-CpG-binding protein 2. Nat Genet. 1999;23:185–8.
2. Chahrour M, Zoghbi HY. The story of Rett syndrome: from clinic to neurobiology. Neuron. 2007;56:422–37.
3. Archer H, Evans J, Leonard H, Colvin L, Ravine D, Christodoulou J, et al. Correlation between clinical severity in patients with Rett syndrome with a p.R168X or p.T158M MECP2 mutation, and the direction and degree of skewing of X-chromosome inactivation. J Med Genet. 2007;44:148–52.
4. Knudsen GP, Neilson TC, Pedersen J, Kerr A, Schwartz M, Hulten M, et al. Increased skewing of X chromosome inactivation in Rett syndrome patients and their mothers. Eur J Hum Genet: EJHG. 2006;14:1189–94.
5. Skene PJ, Illingworth RS, Webb S, Kerr AR, James KD, Turner DJ, et al. Neuronal MeCP2 is expressed at near histone-octamer levels and globally alters the chromatin state. Mol Cell. 2010;37:457–68.
6. Ip JPK, Mellios N, Sur M. Rett syndrome: insights into genetic, molecular and circuit mechanisms. Nat Rev Neurosci. 2018;19:368–82.
7. Tillotson R, Bird A. The molecular basis of MeCP2 function in the brain. J Mol Biol. 2020;432:1602–23.
8. Li CH, Coffey EL, Dall'Agnese A, Hannett NM, Tang X, Henninger JE, et al. MeCP2 links heterochromatin condensates and neurodevelopmental disease. Nature 2020;586:440–4.
9. Ananiev G, Williams EC, Li H, Chang Q. Isogenic pairs of wild type and mutant induced pluripotent stem cell (iPSC) lines from Rett syndrome patients as in vitro disease model. PLoS ONE. 2011;6:e25255.

10. Cheung AY, Horvath LM, Grafodatskaya D, Pasceri P, Weksberg R, Hotta A, et al. Isolation of MECP2-null Rett Syndrome patient hiPS cells and isogenic controls through X-chromosome inactivation. Hum Mol Genet. 2011;20:2103–15.

11. Djuric U, Cheung AY, Zhang W, Mok RS, Lai W, Piekna A, et al. MECP2e1 isoform mutation affects the form and function of neurons derived from Rett syndrome patient iPS cells. Neurobiol Dis. 2015;76:37–45.

12. Kim KY, Hysolli E, Park IH. Neuronal maturation defect in induced pluripotent stem cells from patients with Rett syndrome. Proc Natl Acad Sci USA. 2011;108:14169–74.

13. Li Y, Wang H, Muffat J, Cheng AW, Orlando DA, Loven J, et al. Global transcriptional and translational repression in human-embryonic-stem-cell-derived Rett syndrome neurons. Cell Stem Cell. 2013;13:446–58.

14. Marchetto MC, Carromeu C, Acab A, Yu D, Yeo GW, Mu Y, et al. A model for neural development and treatment of Rett syndrome using human induced pluripotent stem cells. Cell. 2010;143:527–39.

15. Tang X, Drotar J, Li K, Clairmont CD, Brumm AS, Sullins AJ, et al. Pharmacological enhancement of KCC2 gene expression exerts therapeutic effects on human Rett syndrome neurons and Mecp2 mutant mice. Sci Transl Med. 2019;11:eaau0164.

16. Mellios N, Feldman DA, Sheridan SD, Ip JPK, Kwok S, Amoah SK, et al. MeCP2-regulated miRNAs control early human neurogenesis through differential effects on ERK and AKT signaling. Mol Psychiatry. 2018;23:1051–65.

17. Dani VS, Chang Q, Maffei A, Turrigiano GG, Jaenisch R, Nelson SB. Reduced cortical activity due to a shift in the balance between excitation and inhibition in a mouse model of Rett syndrome. Proc Natl Acad Sci USA. 2005;102:12560–5.

18. Nelson ED, Kavalali ET, Monteggia LM. MeCP2-dependent transcriptional repression regulates excitatory neurotransmission. Curr Biol. 2006;16:710–6.

19. Chen WG, Chang Q, Lin Y, Meissner A, West AE, Griffith EC, et al. Derepression of BDNF transcription involves calcium-dependent phosphorylation of MeCP2. Science. 2003;302:885–9.

20. Cohen S, Gabel HW, Hemberg M, Hutchinson AN, Sadacca LA, Ebert DH, et al. Genome-wide activity-dependent MeCP2 phosphorylation regulates nervous system development and function. Neuron. 2011;72:72–85.

21. Deneault E, Faheem M, White SH, Rodrigues DC, Sun S, Wei W, et al. CNTN5(−)(/+)or EHMT2(−)(/+)human iPSC-derived neurons from individuals with autism develop hyperactive neuronal networks. eLife. 2019;8:e40092.

22. Frega M, Linda K, Keller JM, Gumus-Akay G, Mossink B, van Rhijn JR, et al. Neuronal network dysfunction in a model for Kleefstra syndrome mediated by enhanced NMDAR signaling. Nat Commun. 2019;10:4928.

23. Nageshappa S, Carromeu C, Trujillo CA, Mesci P, Espuny-Camacho I, Pasciuto E, et al. Altered neuronal network and rescue in a human MECP2 duplication model. Mol Psychiatry. 2016;21:178–88.

24. Trujillo CA, Adams JW, Negraes PD, Carromeu C, Tejwani L, Acab A, et al. Pharmacological reversal of synaptic and network pathology in human MECP2-KO neurons and cortical organoids. EMBO Mol Med. 2021;13:e12523.

25. McCready FP, Gordillo-Sampedro S, Pradeepan K, Martinez-Trujillo J, Ellis J. Multielectrode arrays for functional phenotyping of neurons from induced pluripotent stem cell models of neurodevelopmental disorders. Biol (Basel). 2022;11:316.

26. Renieri A, Mari F, Mencarelli MA, Scala E, Ariani F, Longo I, et al. Diagnostic criteria for the Zappella variant of Rett syndrome (the preserved speech variant). Brain Dev. 2009;31:208–16.

27. Georgel PT, Horowitz-Scherer RA, Adkins N, Woodcock CL, Wade PA, Hansen JC. Chromatin compaction by human MeCP2. Assembly of novel secondary chromatin structures in the absence of DNA methylation. J Biol Chem. 2003;278:32181–8.

28. Ho KL, McNae IW, Schmiedeberg L, Klose RJ, Bird AP, Walkinshaw MD. MeCP2 binding to DNA depends upon hydration at methyl-CpG. Mol Cell. 2008;29:525–31.

29. Krishnaraj R, Ho G, Christodoulou J. RettBASE: Rett syndrome database update. Hum Mutat. 2017;38:922–31.

30. Agarwal N, Becker A, Jost KL, Haase S, Thakur BK, Brero A, et al. MeCP2 Rett mutations affect large scale chromatin organization. Hum Mol Genet. 2011;20:4187–95.

31. Kudo S, Nomura Y, Segawa M, Fujita N, Nakao M, Schanen C, et al. Heterogeneity in residual function of MeCP2 carrying missense mutations in the methyl CpG binding domain. J Med Genet. 2003;40:487–93.

32. Sheikh TI, Ausio J, Faghfoury H, Silver J, Lane JB, Eubanks JH, et al. From function to phenotype: impaired DNA binding and clustering correlates with clinical severity in males with missense mutations in MECP2. Sci Rep. 2016;6:38590.

33. Buchovecky CM, Turley SD, Brown HM, Kyle SM, McDonald JG, Liu B, et al. A suppressor screen in Mecp2 mutant mice implicates cholesterol metabolism in Rett syndrome. Nat Genet. 2013;45:1013–20.

34. Scala E, Longo I, Ottimo F, Speciale C, Sampieri K, Katzaki E, et al. MECP2 deletions and genotype-phenotype correlation in Rett syndrome. Am J Med Genet A. 2007;143A:2775–84.

35. Mossink B, Verboven AHA, van Hugte EJH, Klein Gunnewiek TM, Parodi G, Linda K, et al. Human neuronal networks on micro-electrode arrays are a highly robust tool to study disease-specific genotype-phenotype correlations in vitro. Stem Cell Rep. 2021;16:2182–96.

36. Hildebrandt MR, Reuter MS, Wei W, Tayebi N, Liu J, Sharmin S, et al. Precision Health Resource of control iPSC lines for versatile multilineage differentiation. Stem Cell Rep. 2019;13:1126–41.

37. Muller FJ, Schuldt BM, Williams R, Mason D, Altun G, Papapetrou EP, et al. A bioinformatic assay for pluripotency in human cells. Nat Methods. 2011;8:315–7.

38. Mekhoubad S, Bock C, de Boer AS, Kiskinis E, Meissner A, Eggan K. Erosion of dosage compensation impacts human iPSC disease modeling. Cell Stem Cell. 2012;10:595–609.

39. Deneault E, White SH, Rodrigues DC, Ross PJ, Faheem M, Zaslavsky K, et al. Complete disruption of autism-susceptibility genes by gene editing predominantly reduces functional connectivity of isogenic human neurons. Stem Cell Rep. 2018;11:1211–25.

40. Zhang Y, Pak C, Han Y, Ahlenius H, Zhang Z, Chanda S, et al. Rapid single-step induction of functional neurons from human pluripotent stem cells. Neuron. 2013;78:785–98.

41. Farra N, Zhang WB, Pasceri P, Eubanks JH, Salter MW, Ellis J. Rett syndrome induced pluripotent stem cell-derived neurons reveal novel neurophysiological alterations. Mol Psychiatry. 2012;17:1261–71.

42. Buzsaki G. Neural syntax: cell assemblies, synapsembles, and readers. Neuron. 2010;68:362–85.

43. Brette R, Gerstner W. Adaptive exponential integrate-and-fire model as an effective description of neuronal activity. J Neurophysiol. 2005;94:3637–42.

44. Ladenbauer J, Augustin M, Obermayer K. How adaptation currents change threshold, gain, and variability of neuronal spiking. J Neurophysiol. 2014;111:939–53.

45. Goffin D, Zhou ZJ. The neural circuit basis of Rett syndrome. Front Biol (Beijing). 2012;7:428–35.

46. Chen X, Han X, Blanchi B, Guan W, Ge W, Yu YC, et al. Graded and pan-neural disease phenotypes of Rett Syndrome linked with dosage of functional MeCP2. Protein Cell. 2021;12:639–52.

47. Ballas N, Lioy DT, Grunseich C, Mandel G. Non-cell autonomous influence of MeCP2-deficient glia on neuronal dendritic morphology. Nat Neurosci. 2009;12:311–7.

48. Williams EC, Zhong X, Mohamed A, Li R, Liu Y, Dong Q, et al. Mutant astrocytes differentiated from Rett syndrome patients-specific iPSCs have adverse effects on wild-type neurons. Hum Mol Genet. 2014;23:2968–80.

49. Mossink B, van Rhijn JR, Wang S, Linda K, Vitale MR, Zöller JEM, et al. Cadherin-13 is a critical regulator of GABAergic modulation in human stem-cell-derived neuronal networks. Mol Psychiatry. 2022;27:1–18.

50. Trujillo CA, Gao R, Negraes PD, Gu J, Buchanan J, Preissl S, et al. Complex Oscillatory waves emerging from cortical organoids model early human brain network development. Cell Stem Cell. 2019;25:558–69.e7.

51. Samarasinghe RA, Miranda OA, Buth JE, Mitchell S, Ferando I, Watanabe M, et al. Identification of neural oscillations and epileptiform changes in human brain organoids. Nat Neurosci. 2021;24:1488–500.

52. McCormick DA, Wang Z, Huguenard J. Neurotransmitter control of neocortical neuronal activity and excitability. Cereb Cortex. 1993;3:387–98.

53. Schmunk G, Gargus JJ. Channelopathy pathogenesis in autism spectrum disorders. Front Genet. 2013;4:222.

54. Rodrigues DC, Mufteev M, Weatheritt RJ, Djuric U, Ha KCH, Ross PJ, et al. Shifts in Ribosome engagement impact key gene sets in neurodevelopment and Ubiquitination in Rett syndrome. Cell Rep. 2020;30:4179–96.e11.

55. Gutkin B, Zeldenrust F. Spike frequency adaptation. Scholarpedia. 2014;9:30643.

56. Sheikh TI, de Paz AM, Akhtar S, Ausio J, Vincent JB. MeCP2_E1 N-terminal modifications affect its degradation rate and are disrupted by the Ala2Val Rett mutation. Hum Mol Genet. 2017;26:4132–41.

57. Fernandes IR, Russo FB, Pignatari GC, Evangelinellis MM, Tavolari S, Muotri AR, et al. Fibroblast sources: where can we get them? Cytotechnology. 2016;68:223–8.

58. Beltrao-Braga PC, Pignatari GC, Maiorka PC, Oliveira NA, Lizier NF, Wenceslau CV, et al. Feeder-free derivation of induced pluripotent stem cells from human immature dental pulp stem cells. Cell Transplant. 2011;20:1707–19.

59. Hotta A, Cheung AY, Farra N, Garcha K, Chang WY, Pasceri P, et al. EOS lentiviral vector selection system for human induced pluripotent stem cells. Nat Protoc. 2009;4:1828–44.

60. Kwiatkowski AV, Rubinson DA, Dent EW, Edward van Veen J, Leslie JD, Zhang J, et al. Ena/VASP is required for neuritogenesis in the developing cortex. Neuron. 2007;56:441–55.

61. Goodman D, Brette R. Brian: a simulator for spiking neural networks in python. Front Neuroinform. 2008;2:5.

ACKNOWLEDGEMENTS

AUTHOR CONTRIBUTIONS

FUNDING

COMPETING INTERESTS

ADDITIONAL INFORMATION